AN EXPLORATORY STUDY ON CONTINUOUS WAVE LASER AND HIGH-SPEED CMOS CAMERA COMBINATION IN PLANAR PARTICLE IMAGE VELOCIMETRY FOR LOW-SPEED FLOWS

by

BUNYAMIN GENCLER

Presented to the Faculty of the Graduate School of
The University of Texas at Arlington in Partial Fulfillment
of the Requirements
for the Degree of

MASTER OF SCIENCE IN AEROSPACE ENGINEERING

THE UNIVERSITY OF TEXAS AT ARLINGTON

August 2019

To my family...

ACKNOWLEDGEMENTS

First of all, I would like to express my gratitude to Dr. Frank K. Lu for giving me the opportunity to work with him and supervising me with his professional and personal advises during my Master's thesis work. I would also like to thank my other committee members Dr. Luca Maddalena and Dr. Donald R. Wilson for their support which enriched this work.

Further, I would like to thank Dr. Andrew Makeev and Dr. Brian Shonkwiler of Advanced Materials and Structures Lab (AMSL) of the University of Texas at Arlington for the loan of the high-speed camera which is one of the key elements of this work.

Furthermore, I would like to the ARC family, which I am honoured to be a member of, for their friendship, support and guidance. Particularly, I would like to thank Ph.D. students Sandeep Eldho James and Rohit Raju Pulimidi for being on the field with their minds and hands whenever I needed. I would like to extend my appreciation to Mr. David Carter for his technical guidance and for providing the safe operation in the ARC.

Lastly, I would like to thank my family, especially to my parents, for raising and supporting me. Without them, I could not even imagine the things I have achieved.

August 30, 2019

ABSTRACT

AN EXPLORATORY STUDY ON CONTINUOUS WAVE LASER AND HIGH-SPEED CMOS CAMERA COMBINATION IN PLANAR PARTICLE IMAGE VELOCIMETRY FOR LOW-SPEED FLOWS

BUNYAMIN GENCLER, M.S

The University of Texas at Arlington, 2019

Supervising Professor: Dr. Frank K. Lu

This study investigates the feasibility of using continuous wave lasers and high-speed CMOS cameras together in 2D particle image velocimetry (PIV) which is a widely-used non-intrusive method in experimental aerodynamics. In order to validate the setup, laminar and turbulent boundary layers over a flat plate with elliptical leading edge are examined in a low-speed wind tunnel. Before the experiments, the suitability of the elliptical-nose flat plate is determined (i.e. pressure gradient over the surface and separation), and the free-stream conditions (flow velocity and test section turbulence) are measured. To strengthen the validation of the setup, numerical simulations are added to the results from the boundary layer theory. The experiments are conducted for two different flow speeds; 4 m/s and 17 m/s with corresponding Reynolds numbers of 72,000, 492,000 respectively. The planar PIV setup is designed following the common practice, and the problems are identified based on the results. Suggestions to improve the setup and possible future work are discussed.

TABLE OF CONTENTS

LIST OF ILLUSTRATIONS

LIST OF TABLES

CHAPTER 1

INTRODUCTION

Particle image velocimetry (PIV) is one of the most common non-intrusive flow diagnostic methods over the decades. Basically, it measures the instantaneous displacements of the particles, which faithfully follow the flow, over the region illuminated by a sheet of laser light. The light scattered from the particles is recorded by an image detector (e.g., photographic film or a digital camera sensor). The recorded image is divided into several sub-regions called interrogation areas (IAs). The particle images are tracked by overlapping the IAs on the next image, and the particles are searched by conducting cross-correlation operations. When the particle location is detected on the next image, a displacement vector is placed. The particle displacement is measured on a plane, and only two components of the velocity, which are the streamwise and the cross-stream components, are obtained. This is known as *planar PIV*. If one more camera is added, the third component of the velocity can be obtained, and this method is called as *stereoscopic PIV*. Three-dimensional velocity vectors can be measured over a volume by using a *volumetric PIV* system.

Even though the accuracy is around $0.2 - 2$ %, which is not as good as single-point measurements like pressure probes and hot-wire anemometry, PIV conveniently maps the flowfield, a procedure that will be time consuming and possibly impossible with point-by-point measurements. Therefore, PIV can instantaneously resolve the boundary interactions and it can determine derived quantities of the flow such as vorticity [5].

In this study, the feasibility of using continuous wave lasers and high-speed CMOS cameras together in a planar PIV setup is examined. Using continuous wave lasers offers a cheaper option. Nowadays, these lasers can supply the necessary power; however, being exposed to that amount of power continuously causes serious problems to be managed such as damage on the materials and exceeding the flammability limit of seeding particles. Moreover, continuous illumination generate particle streaks unlike the particle images in case of using pulsing lasers. The particle streak size is adjusted in this study so that post-processing algorithms for particle images can be used.

A high-speed camera is used in order to increase the sampling rate, hence the frequency response, of the system. Provided that the other elements of the PIV system is properly selected, a high-speed camera is able to capture the time history of the smallest scales in the flow. Specifically, the camera used in this study (*SHIMADZU HYPER VISION HPV-X2*), is able to provide the sampling rate required for the smallest scale even for high-speed flows.

Generally, the laser light sheet is generated by cylindrical lense. In this study, a quartz glass rod is used for this purpose. Due to the potential damage to the glass by the high-powered continuous wave laser, the low-cost and expendable glass rods offer a viable solution.

In order to validate the setup, a flat plate with elliptical leading edge is used in a low speed wind tunnel. Laminar and turbulent boundary layers are examined. To investigate the laminar boundary layer, flow speed is set to 4 m/s and the corresponding $Re = 72,000$. For the turbulent boundary layer, the flow speed is 17 m/s and the corresponding $Re = 492,000$. To check the accuracy of the PIV measurements, the flow over the elliptical flat plate is numerically simulated in *ANSYS Fluent*. Before running the experiments, the flat plate assumption for the elliptical flat plate is

validated using CFD results. The existence of possible separation is checked and the required geometric properties for the elliptical-nose flat plate in order to eliminate the separation is discussed. The test section flow properties of the low-speed wind tunnel used, namely the flow speed, transition Reynolds number and the turbulence intensity, are calculated. Lastly, suggestions to improve the setup are made for future work.

CHAPTER 2

TEST FACILITY

All the experiments in this work were conducted in the Low Speed Wind Tunnel (LSWT) of the Aerodynamics Research Center (ARC) at the University of Texas at Arlington (UTA). The LSWT was designed in 1960s and refurbished in 2006. During this refurbishment, a variable frequency control, 1780 rpm ($\sim$ 60 Hz) Marathon Electric motor was installed.

Figure 2.1: Low Speed Wind Tunnel of the Aerodynamics Research Center at the University of Texas at Arlington

The tunnel is a closed circuit design having a rectangular cross-section except the fan region which is circular. The maximum speed that can be achieved is around 50 m/s and it has 0.6 m $\times$ 0.6 m $\times$ 0.91 m (2 ft $\times$ 2 ft $\times$ 3 ft) test section which means the Reynolds number in the test section may be as high as $\sim 3.5 \times 10^6$ per meter. The LSWT is driven by a fan with 6 blades having NACA 0012 profile, and the fan diameter is 1.83 m (6 ft). Flow inside the tunnel is conditioned by several

screens, turning vanes and honeycomb sections. Depending on the selected screen and honeycomb configuration, turbulence intensity of the tunnel varies between $0.2-1.5\%$. In the following sections §§2.1 and 2.2, velocity measurements and turbulence measurements inside the test section are discussed.

2.1 Velocity Measurements

A pitot-static probe is used to measure the free-stream velocity of the tunnel for different operating frequencies. In order for the flat plate not to be affected by the disturbances generated by the wake of the pitot-static probe, the pitot-static tube was placed lower than the flat plate. Also, it was positioned upstream of the flat plate. Therefore, it is placed 15 cm upstream of the flat plate and 8 cm below the leading edge of the flat plate. This location corresponds to the center point of the tunnel cross-section. In addition to the velocity measurements, a K-type thermocouple is mounted along the side wall of the test section. Figure 2.2 shows the placement of these aforementioned probes. Velocity and temperature data are recorded at the sampling rate of 1000 Hz per channel.

In order to digitize the dynamic pressure readings from the pitot-static probe, a *OMEGA PX653-10D5V* pressure transducer is used. The data from all instruments are acquired by a *National Instruments NI USB-6008* data acquisition board, and recorded with *National Instruments LabVIEW* software. Table 2.1 shows the exact values of the free-stream velocity for each tunnel motor frequency and Figure 2.3 shows the relation between the tunnel motor frequency and free-stream velocity.

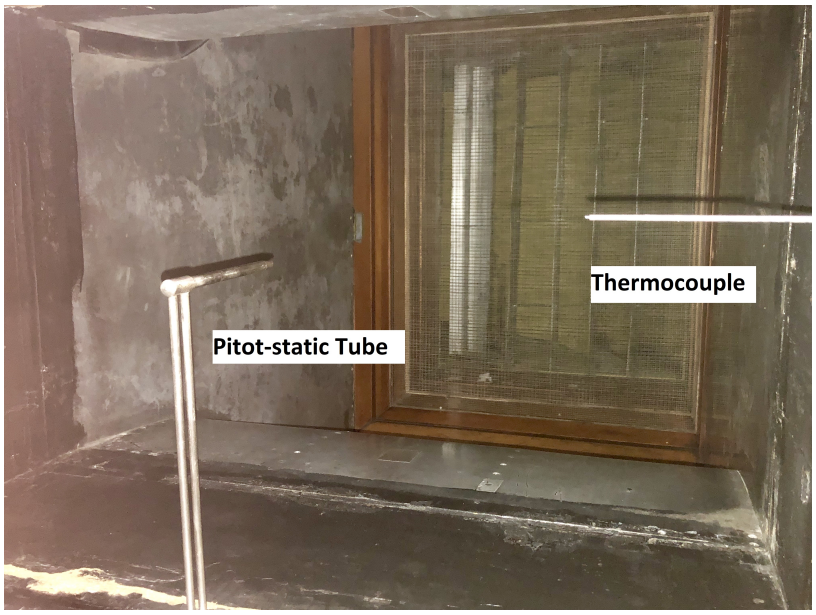

Figure 2.2: Pitot-static probe and K-type thermocouple in the test section

Table 2.1: Tunnel Motor Frequency and Free-stream Velocity

Tunnel Motor Frequency $[Hz]$	**Freestream Velocity** $[m/s]$
5	3.9
10	8.12
15	12.37
20	16.9
25	20.8
30	24.9
35	28.9

2.2 Test Section Turbulence

Test section turbulence is an important parameter and should be known beforehand because the disturbances in the free-stream flow is a mechanism that can trigger early transition. Especially, for this experiment which is a boundary-layer survey, free-stream turbulence intensity is expected to have a significant effect on Re_{tr}. Since one purpose of this work is to be able to observe a turbulent boundary layer, Re should be set accordingly such that it is greater than Re_{tr}. Van Driest and

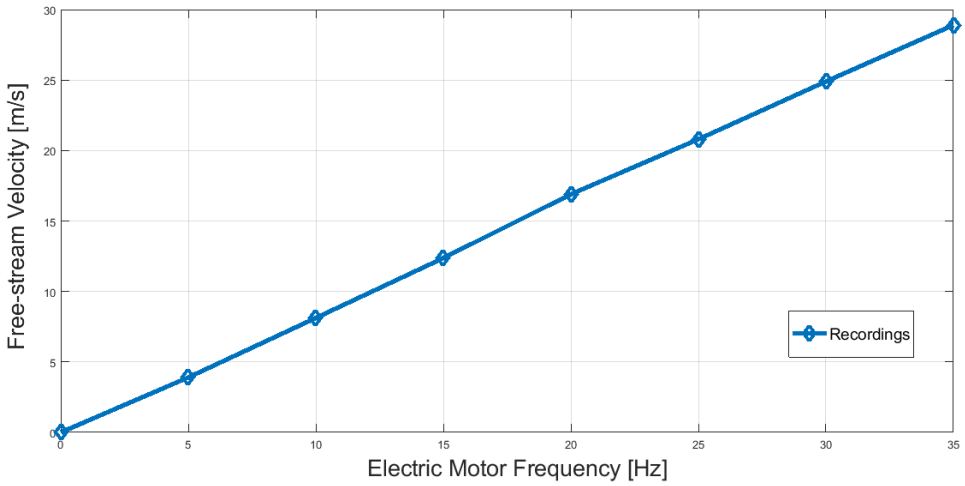

Figure 2.3: Tunnel motor frequency vs free-stream velocity

Blumer, formulated a relation between Re_{tr} and free-stream turbulence intensity for a low-speed flow over a flat plate [1],

$$1690/Re_{tr}^{1/2} = 1.0 + 19.6\,\mathrm{Re}_{tr}^{1/2}\,(u'/U)^2 \tag{2.1}$$

where (u'/U) is the free-stream turbulence intensity. The relation given by Eq. 2.1 is illustrated in Figure 2.4. As a result, the free-stream turbulence intensity is required in order to determine Re_{tr}.

The test section turbulence of the LSWT was determined by Seath and Fairchild [3] for different screen and honeycomb arrangements by using a turbulence sphere (Figure 2.5). The turbulence sphere is an aerodynamically smooth, 4-inch diameter duckpin ball which has four equally spaced holes on the aft surface and two holes on the front stagnation point to measure the pressure. These holes are connected to a manometer. The average of four pressure values on the aft surface is subtracted from the stagnation value to determine ΔP. Then, it is divided by the test section dynamic pressure for each Re. The Reynolds number corresponding to $\Delta P/q = 1.22$

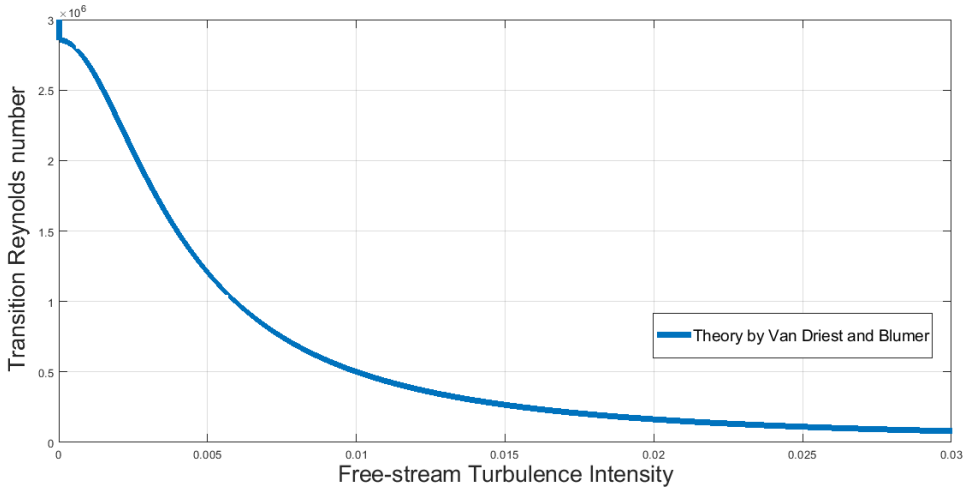

Figure 2.4: Effect of free-stream turbulence on transition Reynolds number [1]

is called the critical Reynolds number (Re_{cr}). *"Free-Air"* Re_{cr} is given as $385,000$. In order to get the *Tunnel Turbulence Factor (TTF)*, Re_{cr} is divided into the free-air value. An example TTF calculation is shown in Figure 2.6 which is the case when all screens and honeycombs are installed onto the LSWT.

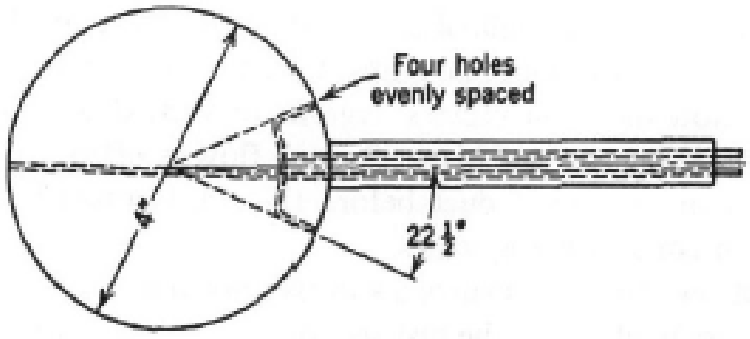

Figure 2.5: Turbulence Sphere (taken from [2])

The LSWT has four upstream slots for screens and honeycombs. Besides, the corner after the diffuser section may be covered with aluminum screens. If one side of

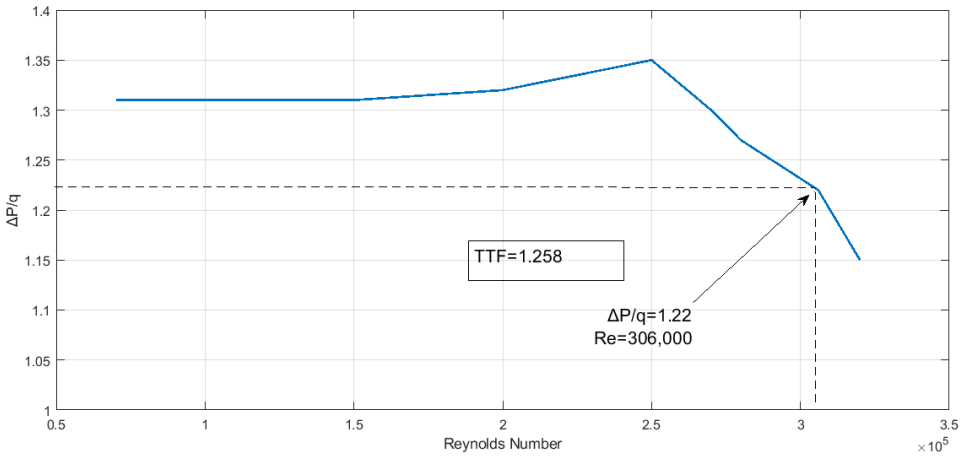

Figure 2.6: An example tunnel turbulence factor calculation when all screens and honeycombs are installed [3]

the corner is covered, it is called "half", and if both sides of the corner are covered, it is called "full". Figure 2.7 illustrates the upstream slots and Table 2.2 shows the screen and honeycomb descriptions. In addition, Table 2.3 shows the TFF results conducted by Seath and Fairchild [3] for different screening settings.

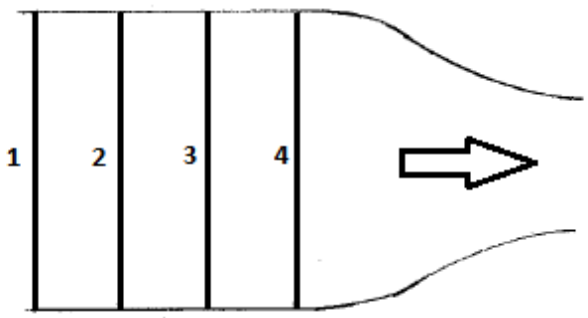

Figure 2.7: Upstream Screen and Honeycomb Slots

In this work, the LSWT has the following set of screens at designated locations. At Slot 1 and Slot 2 (Figure 2.7), "a" from Table 2.2 is used. At Slot 3, "b" is located, and the diffuser corner is half covered. This configuration lies between Test 7 and

Table 2.2: Screen and Honeycomb Descriptions

Symbol	**Screen and Honeycomb Descriptions**
a	1/2 inch mesh hardware cloth, 0.041 inch diameter wire
b	1/4 inch mesh hardware cloth, 0.041 inch diameter wire
c	Galvanized window screening, 14x18 wires per inch, 0.011 inch wire diameter
d	Aluminum Window Screening
h	Honeycomb, 1/8 inch hexagonal cells, 1 inch deep

Table 2.3: Tunnel Turbulence Factor (TTF) Results [3]

Test Number	**TTF**	**Upstream Position Slots**				**Diffuser Screen**
		1	**2**	**3**	**4**	
1	1.258	a	b+h	c	d	**Full**
2	1.305	-	-	-	b+h	**Full**
3	1.350	-	-	b+h	-	**Full**
4	1.426	-	b+h	-	-	**Full**
5	1.640	a	b	c	d	**Full**
6	1.780	a	-	c	d	**Full**
7	1.950	a	-	c	-	**Half**
8	2.040	-	-	c	-	**Half**

Test 8 in Table 2.3. Therefore, TTF can be taken as **2**. However, turbulence intensity is required to determine Re_{tr}. Therefore, TTF and turbulence intensity are related. Using hot-wire anemometry, this relation was determined by Dryden et al. [6] and Dryden and Kuethe [7]. Figure 2.8 taken from [2] shows this relation.

Considering TTF values from Table 2.3, the turbulence intensity of the LSWT varies between $0.2 - 1.5\%$. Particularly, for the screening configuration used in this work, the turbulence intensity corresponds to **1.2%**. Since the turbulence intensity is independent of speed if the screens, turning vanes, honeycombs etc. are used to regulate the turbulence [6], the turbulence intensity of the LSWT is independent of speed and it stays constant. Then, using Eq. 2.1, Re_{tr} is calculated as **380,000**. Having $Re_{tr} = 380,000$, it can be stated that in Case I, the boundary layer will be *laminar*, and in Case II, the boundary layer will be *turbulent*.

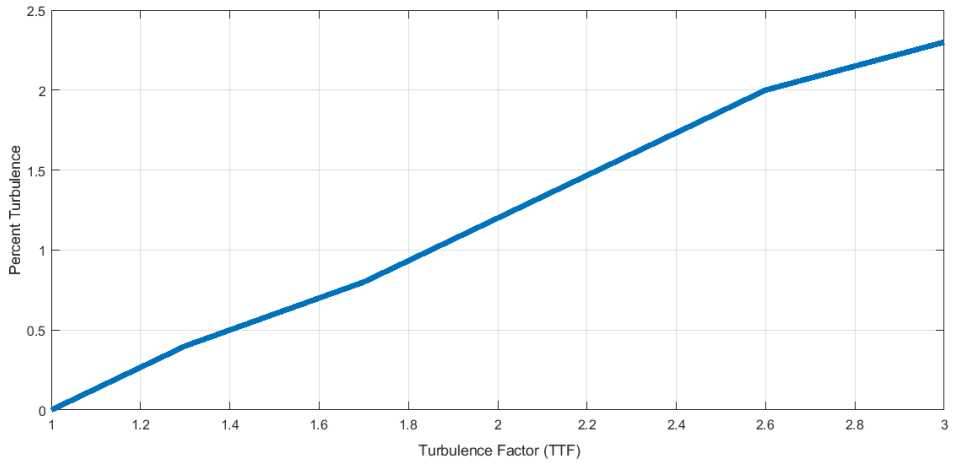

Figure 2.8: Variation of turbulence factor with turbulence intensity from hot-wire anemometry measurements

Another important parameter is the length scale of the turbulence. Dryden et al. showed that, if the guide vanes are arranged as the way the LSWT has (i.e. turning vanes, screens and honeycombs), the length scale of turbulence equals to the size of the grid cells [6]. In case of this study, the smallest cell size is 6.35 mm (1/4 inch). Therefore it can be taken as the length scale of the free-stream turbulence. Turbulence length scale and turbulence intensity parameters are used in the numerical simulations to model the free-stream conditions. Furthermore, Eq. 2.1 relies on the assumption that the length scale and the boundary layer thickness should have the same order of magnitude [1]. In Chapter 4, the boundary layer thickness is calculated numerically, and in Chapter 6 it is obtained from PIV results. Both results show that turbulence length scale and boundary layer thickness values have the same order of magnitude. Hence, the assumption made by Van Driest and Blumer in order to derive Eq. 2.1 is valid for this work.

CHAPTER 3

ELLIPTICAL-NOSE FLAT PLATE

Flat plates having sharp or bluff leading edges are susceptible to disturbances in the flow, and sensitive to flow misalignments i.e. angle of incidence. Hence, the flow may separate and become turbulent before the re-attachment to the surface [8]. Therefore, as a common practice, a flat plate with an elliptical leading edge is used during the experiments. Figure 3.1 shows the drawing of the elliptical-nose flat plate, and Figure 3.2 shows it inside the test section. The elliptical-nose flat plate is made of aluminum and, the dimensions are 500 mm in length, 724 mm in width and the thickness is 32 mm. The elliptical part has a semi-major axis length of 100 mm and a minor axis length of 32 mm.

The point where the elliptical part and the flat surface join is called the junction. If certain design rules for the shape of the ellipse are not followed, adverse pressure gradient near the junction cause separation [4].

Narasimha et al. [4] studied the effect of nose shape factors on the separation tendency, and provided a correlation between the shape parameters and separation. If the nose shape is an ellipse, the equation for the curve is given by,

$$[(a-x)/a]^n + (y/b)^n = 1, \quad 0 \leqslant x \leqslant a \quad n > 2 \tag{3.1}$$

where a is the length of the nose (i.e. semi-major axis length), b is the nose thickness (i.e. minor axis length). Then the separation tendency is plotted with respect to the shape parameters. The flat plate used in these experiments has $a/2b = 3.2$ and $n = 2.87$ which is shown in Figure 3.3 as a black diamond which lies in the "no

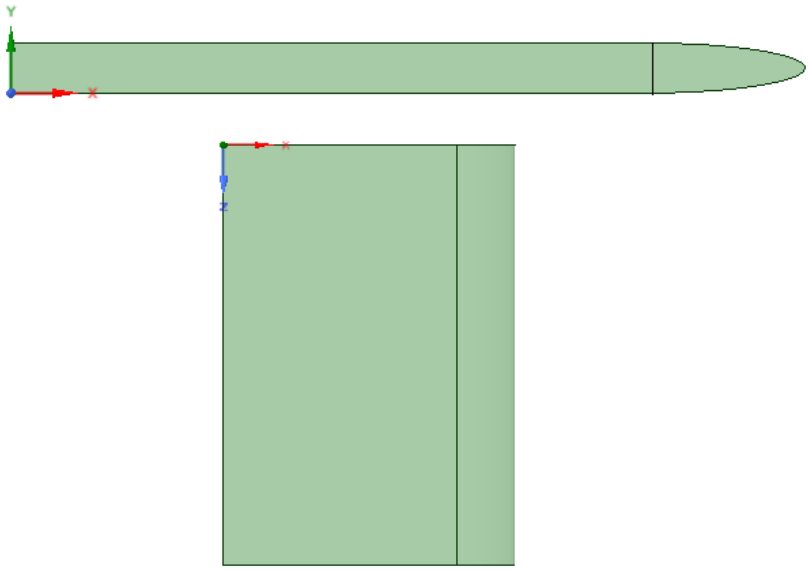

Figure 3.1: Elliptical-nose flat plate drawing

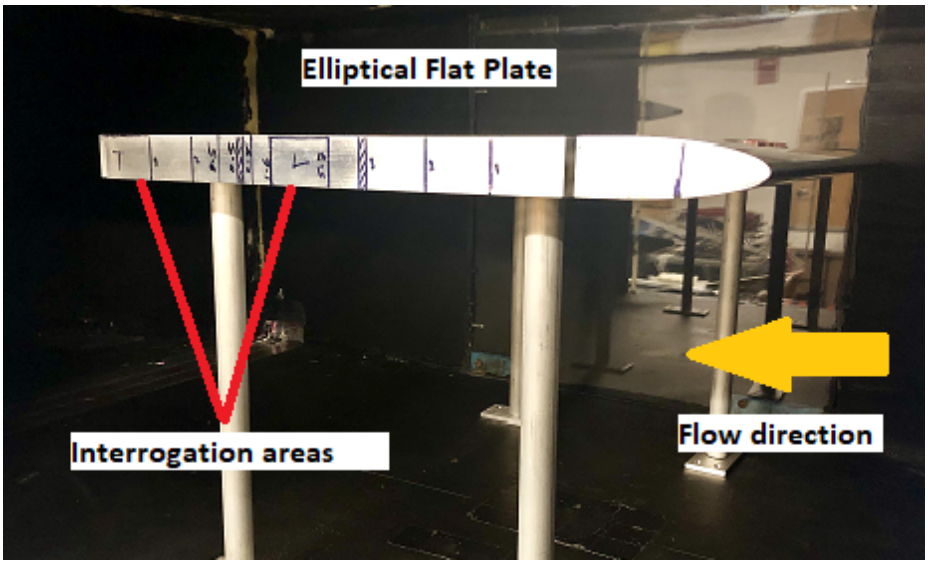

Figure 3.2: Elliptical-nose flat plate in the test section

separation likely zone". Hence, it is validated that no separation will be observed around the junction during the experiments.

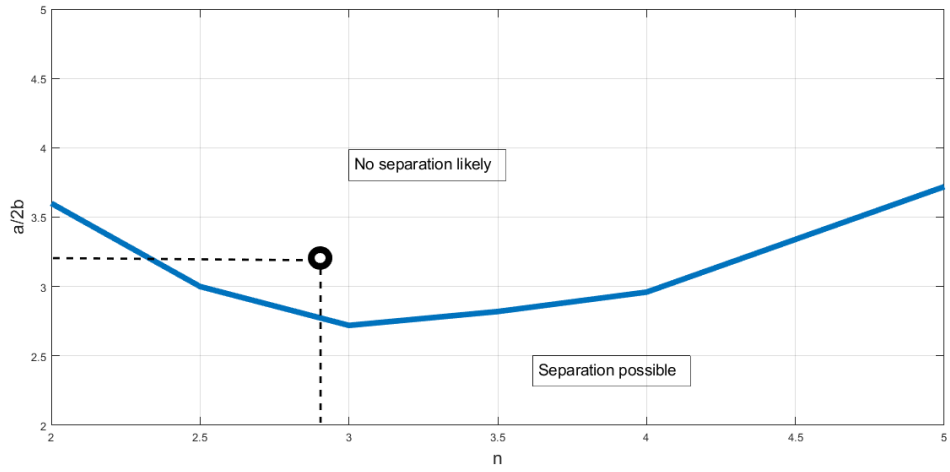

Figure 3.3: The boundary between separated and unseparated flow with respect to shape parameters [4]

In order for the flat plate assumption to be valid, the pressure gradient along the streamwise axis $\frac{\partial p}{\partial x}$ has to be zero. The flow over the elliptical-nose flat plate is numerically simulated in *ANSYS Fluent* for these cases, one in which the free-stream velocity is 4 m/s and the other one with 17 m/s. Details on the numerical simulations in *ANSYS Fluent* are discussed in the Chapter 4.

Differential pressure contours relative to the inlet are plotted and the results for 4 m/s and 17 m/s cases are shown in Figures 3.4 and 3.5 respectively. Yellow rectangles in Figures 3.4 and 3.5 indicates the regions of interest (ROI).

For detailed observation, differential pressure values and pressure gradient along the streamwise axis on the wall surfaces are plotted. The differential pressure is the pressure value relative to the free-stream pressure at the inlet. Figure 3.6 shows the differential pressure values on the flat plate surface vs streamwise location, and the dashed rectangles represent the ROI for each case. Figure 3.7 shows the pressure gradient along the streamwise axis vs streamwise location, and the blue dashed rectangle indicates the ROI for 4 m/s case as the red dashed rectangle represents the ROI for

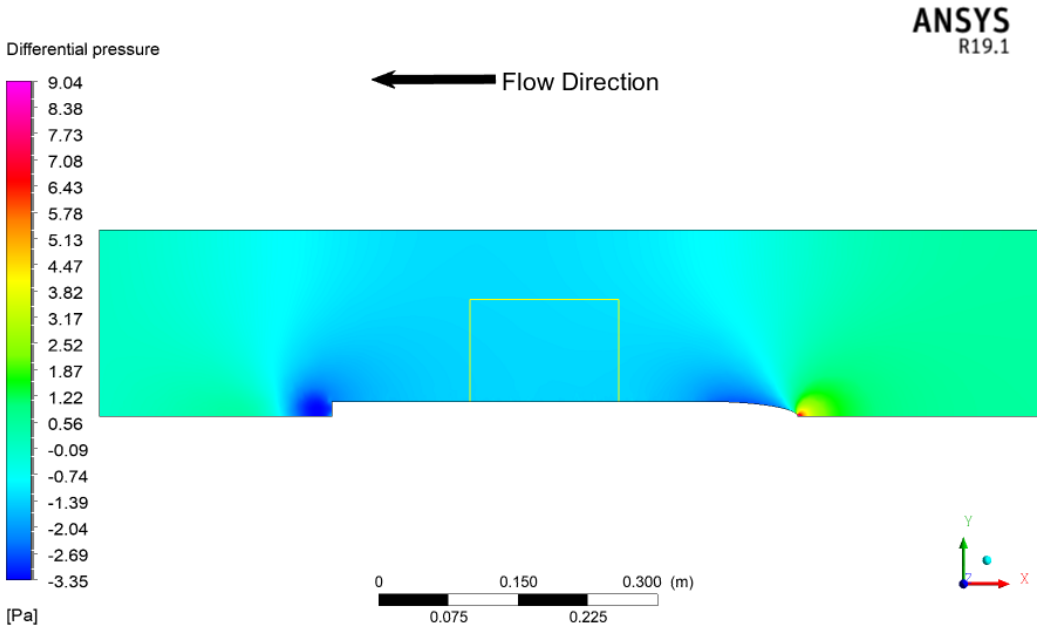

Figure 3.4: Differential pressure contour relative to the inlet (4 m/s)

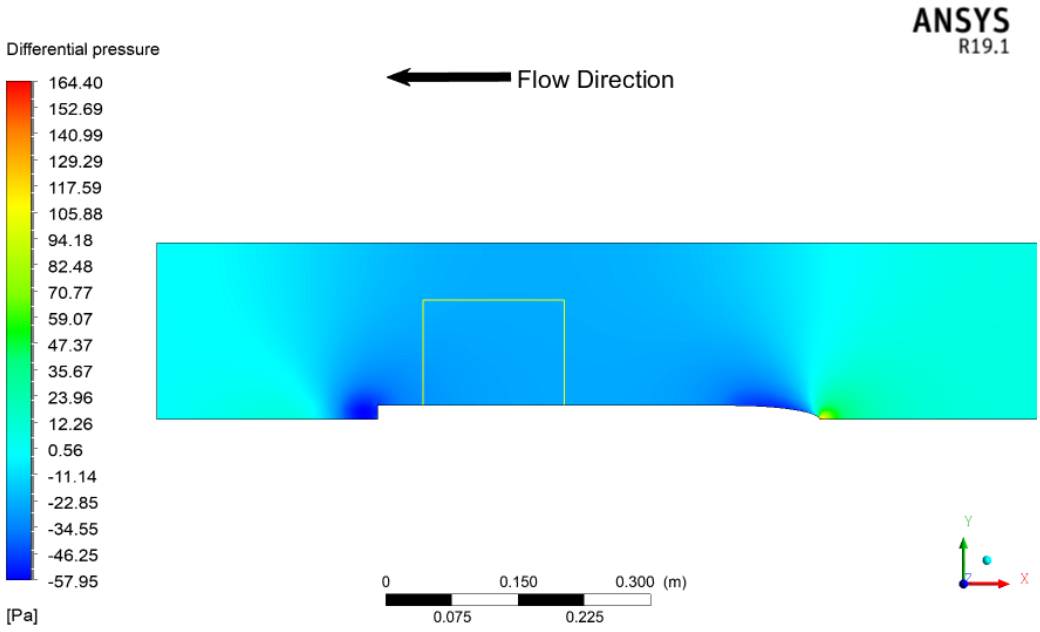

Figure 3.5: Differential pressure contour relative to the inlet (17 m/s)

17 m/s case. Besides, the drawing of the elliptical-nose flat plate is added to each plot.

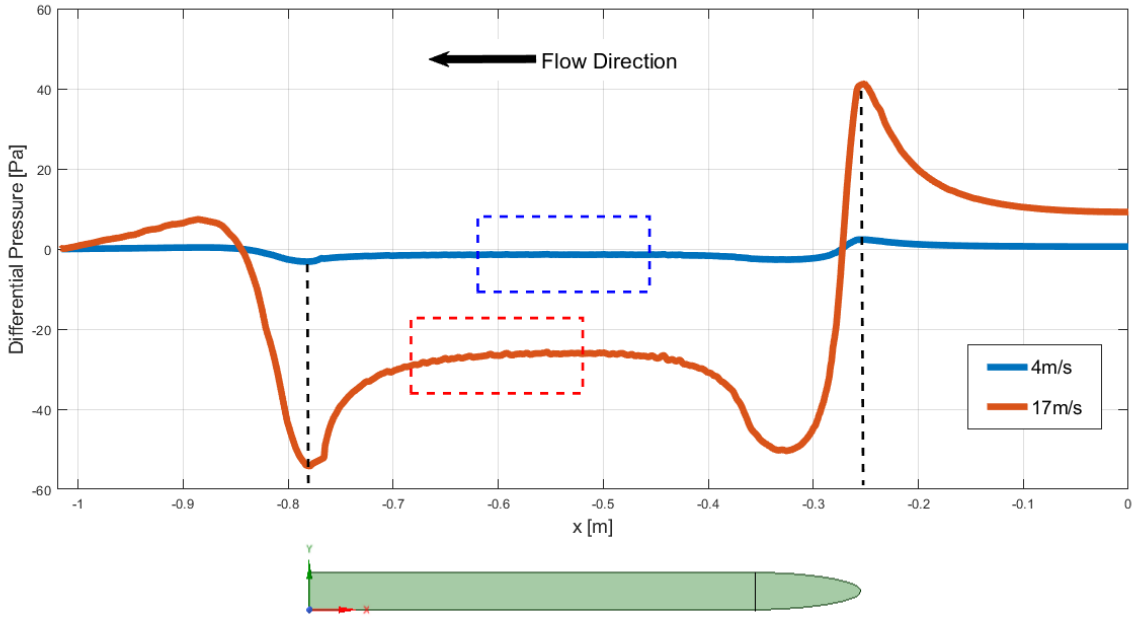

Figure 3.6: Pressure over the flat plate surface

For the 4 m/s case, pressure is constant along the streamwise axis and the pressure gradient along with it is practically zero. The same statement can be made for the 17 m/s case; however, close to the end of ROI, pressure value changes and an increase in the pressure gradient is observed. This is caused by the trailing edge vortex generated by the blunt trailing edge of the flat plate. This problem can simply be avoided by moving the ROI closer to the leading edge; however, the transition Reynolds number (Re_{tr}) should be considered since the Reynolds number based on the streamwise location (Re_x) decreases as ROI moves towards the leading edge, and if Re_x is smaller than Re_{tr}, only laminar boundary layer can be observed.

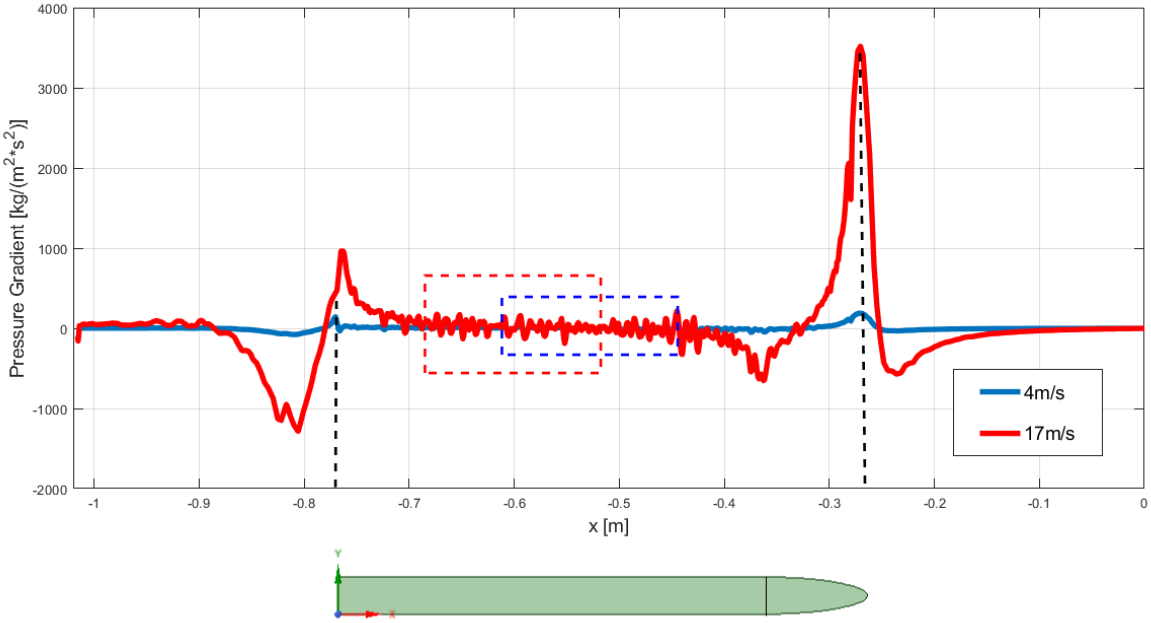

Figure 3.7: Pressure gradient over the flat plate surface

CHAPTER 4

SIMULATIONS

Before PIV experiments, the flow over the elliptical-nose flat plate is numerically simulated, and the results are used to validate the experimental results. In addition to that, numerical simulations give the researchers an idea of the possible outcome. For all numerical simulations in this work, *ANSYS Fluent 19.1* is used, and cases I and II are modeled in the selected domain shown in Figure 4.1. The computational domain is decided to be a 2D rectangle since the images from planar PIV are rectangles. The domain is 1000 $mm \times 200$ mm rectangle, and the bottom surface is modified in order to represent the elliptical-nose flat plate. There are $250mm$ long spaces are left ahead and behind the plate. Since the PIV interrogation area is 100 mm above the surface of the flat plate, the height of the computational domain is kept as 200 mm in order to reduce the effect of the top wall of the test section. Edges of the domain are named accordingly and different flow and surface conditions are defined on the edges.

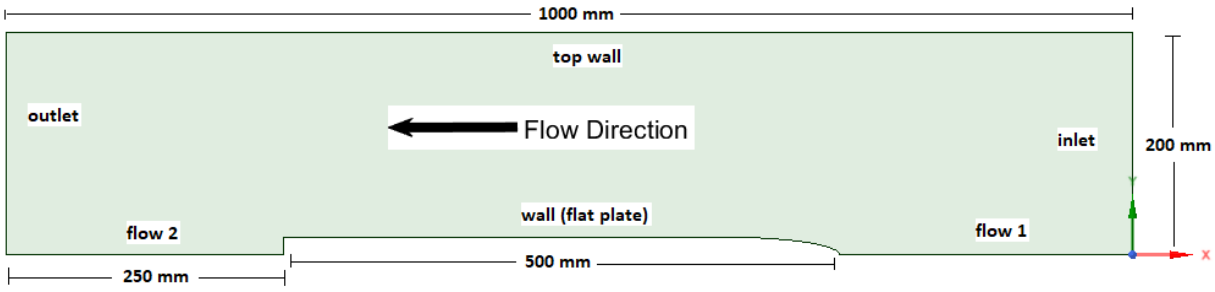

Figure 4.1: Calculation domain

The edge named as *wall (flat plate)* represents the elliptical part, flat surface and the back wall of the flat plate, and defined as a wall with no-slip condition. As their names refer, *inlet* and *outlet* represents the inlet and the outlet of the domain, and they are defined as the velocity inlet and the pressure outlet respectively. The edge *top wall* may seem to represent the top wall of the test section; however, the top test section wall is 23 cm away from the surface of the flat plate where as the edge *top wall* is nearly 18 cm away from the flat plate surface. In other words, the edge *top wall* is selected so that it is away from the tunnel boundary layer. Edges *top wall*, *flow 1* and *flow 2* are defined as walls with zero shear. Not including the tunnel wall causes errors in the calculated velocity. However, when the velocity measurements on the flat plate are checked, the error is determined as $\sim 2\%$. Since simulating the boundary layer on the test section wall means extension of the calculaton domain, new mesh structure, additional calculation time and further considerations, the error is accepted.

In order to generate the mesh structure, all the edges are divided into small pieces called divisions. The number of divisions on each edge are tabulated in Table 4.1. The mesh shown in Figure 4.2 has 12,088 nodes.

Table 4.1: Number of Divisions on the Edges

Edges	***wall***	***inlet***	***outlet***	***flow 1***	***flow 2***	***top wall***
Number of Divisions	516	200	200	250	250	300

To model the free-stream turbulence, the k–ε model with the enhanced wall treatment option is used with the turbulence intensity and the turbulence length scale determined in Chapter 2. *"SIMPLE"* is selected as the solution method, and the spatial discretization selections are tabulated in Table 4.2. One thousand iterations

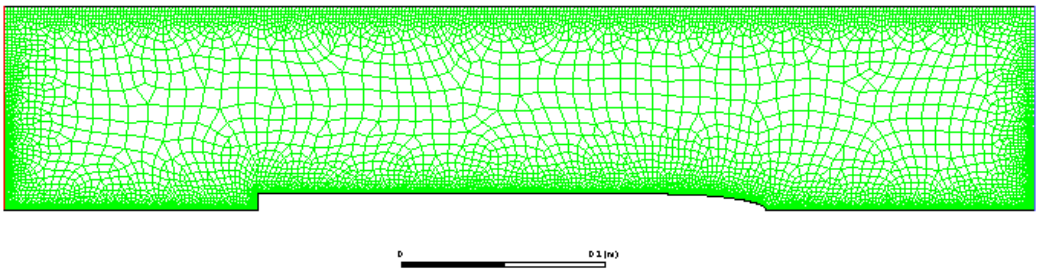

Figure 4.2: Mesh Structure

are made in order to get a convergent solution while residuals are defined as 10^{-5}. After several of runs, even if the number of iterations is set to 1000, the converged solution usually does not require that many iterations. As a result, Figures 4.3 and 4.4 shows the velocity contours for Cases I and II respectively. Further, Figures 4.5 and 4.6 illustrate the velocity vectors for Cases I and II respectively. Furthermore, in Chapter 3, Figures 3.4 and 3.5 displays the differential pressure contours over the elliptical-nose flat plate for the given cases.

Table 4.2: Spatial Discretization

Spatial Discretization	**Method**
Gradient	Least Squares Cell Based
Pressure	Second-Order
Momentum	Second-Order Upwind
Turbulent Kinetic Energy	First-Order Upwind
Turbulent Dissipation Rate	First-Order Upwind

Although the Cases I and II are nominally 4 m/s and 17 m/s respectively, these values are obtained from pitot-static tube measurements ahead of the flat plate. Due

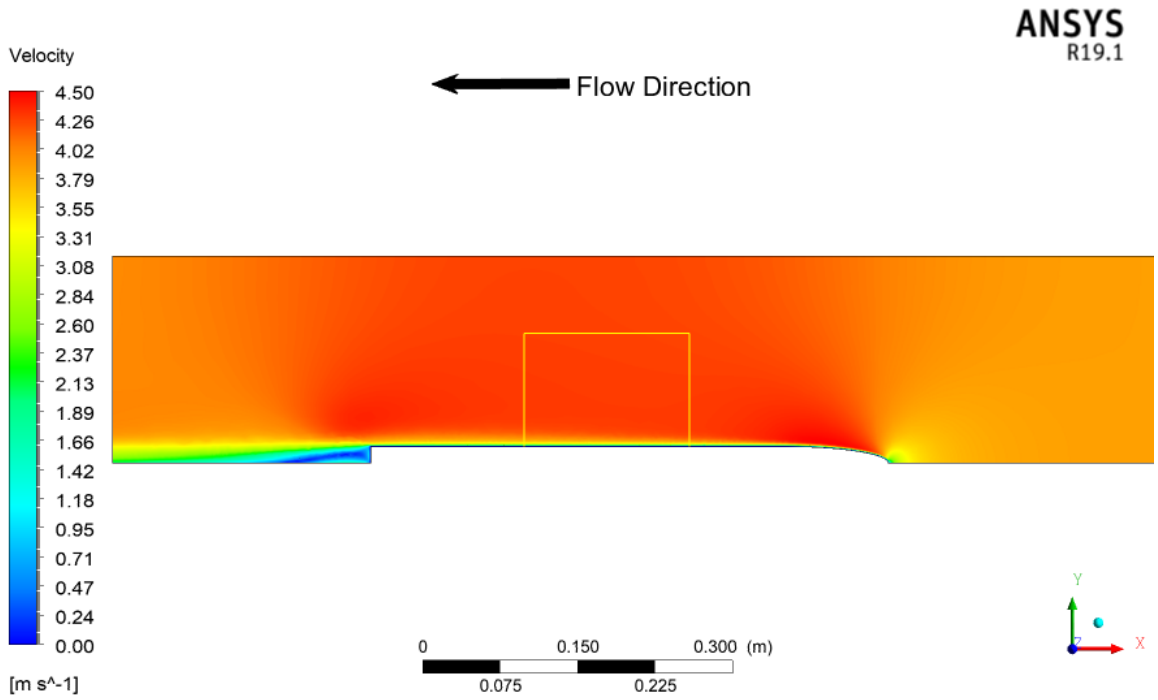

Figure 4.3: Velocity contour for case I (4 m/s)

to the convergent shape of the elliptical flat plate and the boundary layers on the flat plate and top tunnel wall, the flow faces a narrower area; therefore, the flow speed increases. According to the measurements obtained on the flat plate, Case I corresponds to 4.63 m/s and Case II corresponds to 19.55 m/s. These values are expected to be obtained from PIV results.

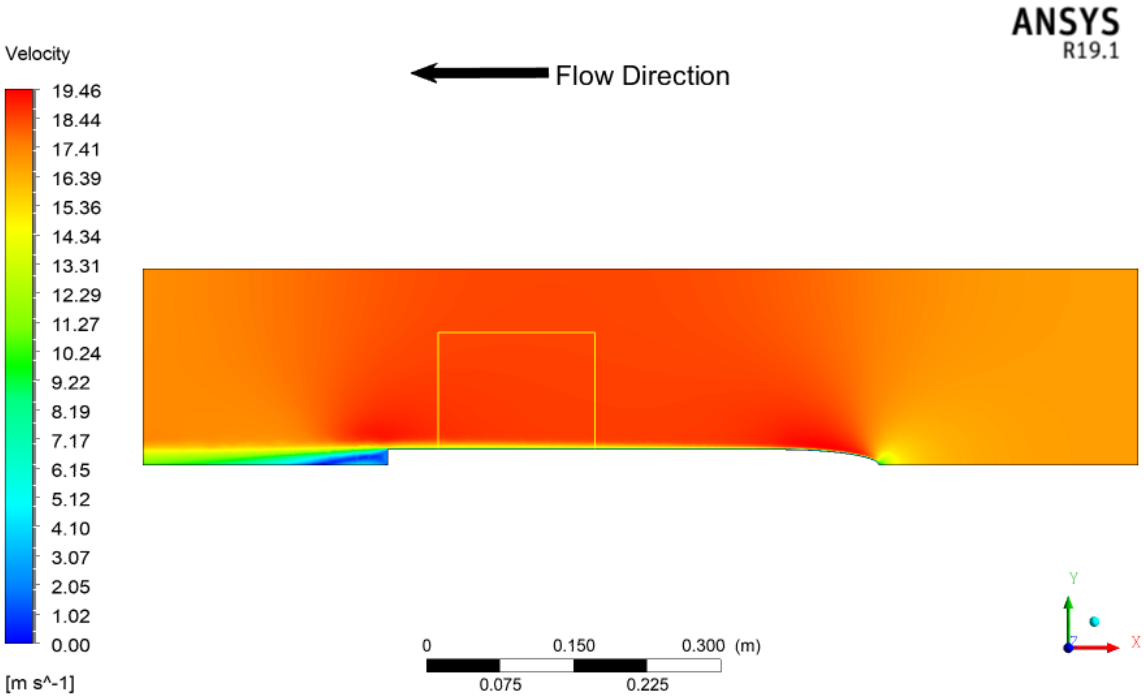

Figure 4.4: Velocity contour for case II (17 m/s)

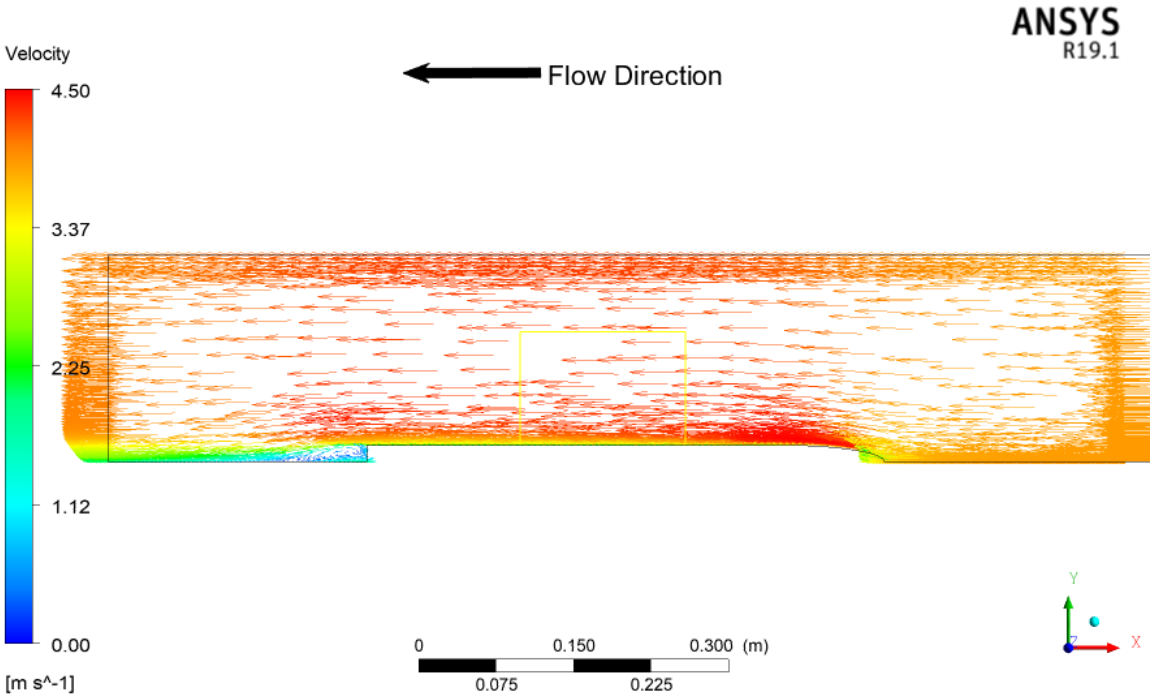

Figure 4.5: Velocity vectors for case I (4 m/s)

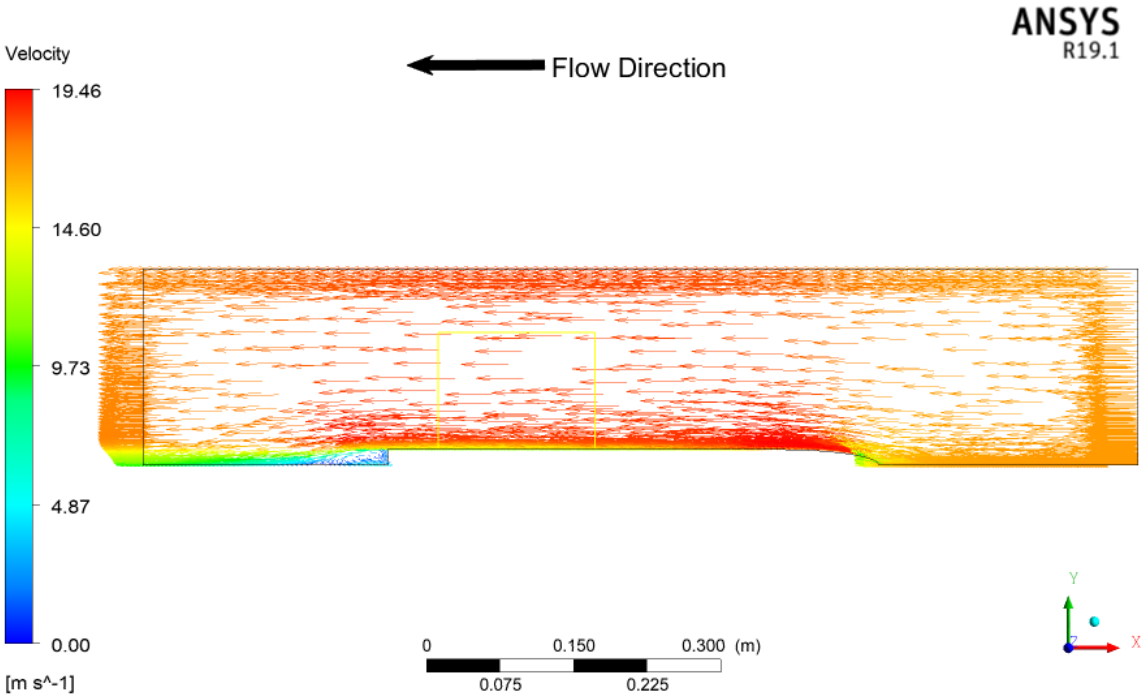

Figure 4.6: Velocity vectors for case II (17 m/s)

CHAPTER 5

DESIGN OF 2D PIV EXPERIMENT

The main difference of the PIV method developed in this study is the combination of a continuous wave (CW) laser and a high-speed CMOS camera. Although the CMOS high speed cameras are used in many studies, CW lasers are not common due to several reasons like continuous exposure of high laser energy onto the test object and particle streaks in the images. The experimental setup used in this study is shown in Figure 5.1

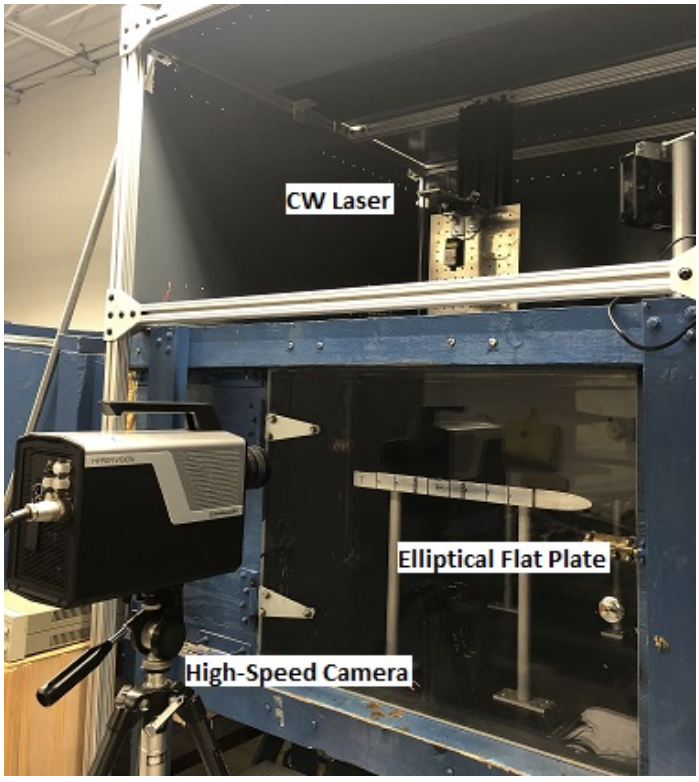

Figure 5.1: PIV setup on the LSWT

The PIV system of this study has a 0.5 W continuous wave laser having the wavelength of 405 nm, and with variable beam diameter which is set to be 0.5 mm for Case I and 1.5 mm for Case 2. For the imaging system, a *SHIMADZU HYPER VISION HPV-X2* high-speed camera is used with a *NIKON* 18-70 mm f/3.5-4.5G ED IF AF-S DX Nikkor Zoom Lens. Olive oil is used to seed the flow, and atomized olive oil particles having 1 μm diameter are generated by *The LaVision Aerosol Generator*. The laser beam is converted to a laser sheet by a 10 mm diameter rod lens made of quartz. The laser sheet thickness is equal to the diameter of the incoming laser beam which is 0.5 mm and 1.5 mm for Cases I and II respectively. Since the aim of this study is to capture the time history of the smallest eddies in the flow, instantaneous images are recorded at 150 Hz, 3 kHz and 13 kHz for Case I , and 650 Hz, 3 kHz, 13 kHz and 54 kHz for Case II. *OpenPIV* software is used to process the data [9]. In order to calculate the particle displacement, cross-correlation operations are conducted on a designated interrogation area (IA). In the first pass, 64 $\times$ 64 px^2 IA is used with 50% overlap; then, in the second pass, 32 $\times$ 32 px^2 IA is used with 50% overlap. Details of the design features of the PIV system developed in this study are examined in the subsequent sections.

5.1 Interrogation Area

The cross-correlation operation is done on a limited area in the ROI. This area is called the interrogation area (IA). IA calculates the matching degree of two exposures in order to calculate the displacement of the particle images. Also, IA acts like a spatial filter and limits the minumum scale to be captured. Usually, the wave number corresponding to the smallest scale, which is the Kolmogorov scale where $k = 2\pi/\eta$. However, size of the IA (Δ_{IA}) limits the wave number, and when the Nyquist criterion is fulfilled, the limit wave number is calculated as $k = \pi/\Delta_{IA}$ [10].

The cross-correlation operation is done in two passes. One is with 64 $\times$ 64 px^2 IA 50% overlap and the second is with 32 $\times$ 32 px^2 IA is used with 50% overlap. The camera with $32\mu m$ sensor size and 400×250 pixels probes the ROI of 160 $mm \times$ 100 mm. This ROI size gives the magnification factor of 0.16. Particle's diameter (d_p) and the particle image diameter (d_t) are not equal and they are related by Bastiaans using light diffraction theory for small particles [11];

$$d_t \cong \sqrt{M^2 d_p^2 + \left(2.44(1+M)f^{\#}\lambda\right)^2} \tag{5.1}$$

where M is the magnification factor, d_p is the particle's physical diameter, d_t is the particle image diameter, $f^{\#}$ is the f-number and λ is the wavelength. The pixel size is equal to 0.4 mm in this configuration. This value gives the particle displacement is less than 1–2 pixels for Case I and less than 3–4 pixels for Case II. Having 1-2 pixels of displacement means that the uncertainty may be in the order of a fraction of a pixel which can not be measured by a digital camera. To solve this problem and measure the fractional values of the displacement, the correlation peak is interpolated with a curve fit. When the sub-pixel interpolator fails, the curve fit algorithm biases fractional displacements to integer pixel values. This phenomenon is called "*peak locking*," and it is a major limitation in PIV. One possible solution to this problem is to increase the particle image diameter so that $d_t > 2$ pixels [12]. According to Equation5.1, the particle image size requirement is satisfied for the given setup. Since d_t can further be increased by increased sampling rate [12], the histograms of the actual PIV displacement of the higher sampling rates are not analyzed.

Table 5.1: Sampling rates for each case

Velocity	**Sampling Rate**		
	IA	**Intermediate**	**Kolmogorov Scale**
4 m\s	150 Hz	3 kHz	13 kHz
17 m\s	650 Hz	3 kHz & 13 k Hz	54 kHz

5.2 Sampling Rate

The highest sampling rate is necessary in order to capture the smallest scale of the flow, called as Kolmogorov scale η. Since the integral scale of the flow is determined in Chapter 2, the following relation can be made;

$$\frac{\eta}{L} \approx Re^{-3/4}$$

where L is the integral scale of the flow and Re is the Reynolds number. In order to capture the Kolmogorov scale, the corresponding wave number is to be known. For a normalized energy spectra, Kolmogorov scale has the wave number of 10^4 [13]. Since

$$k = \frac{2\pi SR}{U}$$

where SR is the sampling rate and U is the free-stream velocity, required sampling rate values for each case are calculated. Then, the calculated sampling rate values are doubled in order to fulfill the Nyquist criterion. The smallest sampling rate is determined by the IA as discussed in the previous section. IA acts as a spatial filter and sets the wave number as 245. Besides the calculated sampling rates, data is recorded at 3 kHz as well. Even though the sampling rate set by IA gives the most accurate results, the higher sampling rates are measured to show the capabilities of the camera and estimate the possible error.

Since the laser is continuous, synchronization between the laser and the camera,which can be a tedious chore in PIV systems with pulsing lasers, is not required. Therefore, the camera recording rate can be taken as SR.

5.3 Illumination

Unlike the common practice, which is using a pulsing laser and combination of cylindrical lenses, a CW laser and a quartz glass rod is used in this study. Detailed design criterion and features are discussed below in the corresponding sections.

5.3.1 Continuous Wave Laser

As a light source, 0.5 W CW laser with 405 nm wavelength (purple) is used. The laser has variable beam diameter, and it is set to be 0.5 mm for Case I and 1.5 mm for Case II. A shutter is required for the CW laser in order to freeze the image but if the time between two subsequent images is in the order of micro-seconds or lower, the camera itself acts like a shutter [5]. The downside of using a CW laser is to control continuous energy coming to the equipments and to the region of interest (ROI). Since the laser is triggered with the camera, operation time can be go up to 1 second even though the recording time is in the order of microseconds. If the seeding particles are gases, liquids or bubbles, the laser can easily evaporate the particles or, more dangerous than that, it may cause an ignition. Besides, the laser heats up surfaces which changes surface properties; for instance, in this study, increased surface temperature changes the boundary layer profile over the flat plate. In order to assure safety of the experiment, laser induced damage threshold (LIDT) of all equipments interacting with the laser has to be checked. Coated optical elements are required. Most importantly, flammability limit of the seeding particles must be considered along with the seeding density. Based on the experience gained during this study, laser power up to 2 W is acceptable with the given equipments and seeding condition. Even though the 0.5 W laser is safe to use, it is later noticed that the power is not enough to scatter sufficient light from the particles. An attempt is made to address this issue through design of the setup.

In order to mount the laser on the test section, a special holder is designed and manufactured. There are two ways to adjust the position of the laser. One is using the rails for coarse adjustments, and the second one is small moving plates on the holder for fine adjustments. All in all, the holder allows the laser to move in all three axes with millimeter accuracy. There are several locations on the holder plate for the optical elements. Figure 5.2 shows the laser holder with optical elements. As it can be seen in Figure 5.2, the frame is covered in order to avoid any damage caused by the reflected light, and a cooling fan is added. Due to continuous illumination, particles are recorded as particle streaks on the image plane.

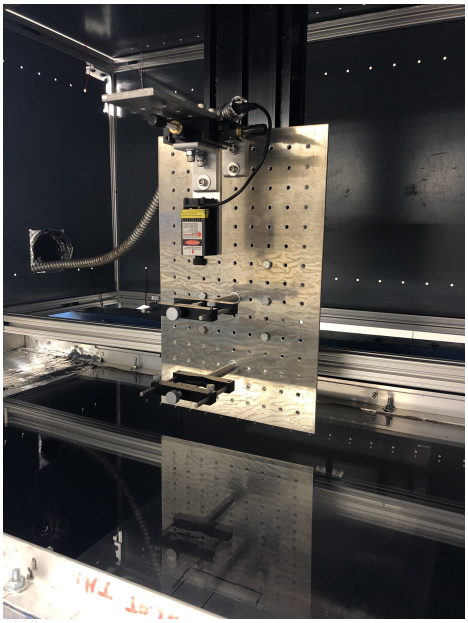

Figure 5.2: Laser holder on the test section

5.3.2 Light Sheet Optics

To probe the 160 mm $\times$ 100 mm ROI, the laser sheet is generated via expansion of the laser beam by a glass rod instead of combinations of cylindrical lenses. A quartz

glass rod is used because of its heat resistance. To achieve required divergent angle, the diameter of the rod is chosen as 10 mm. The focal length approximately equals to the diameter. Laser sheet thickness is equal to the beam diameter; hence, it is 0.5 and 1.5 mm for Cases I and II respectively. Since the off-plane velocity component in this experiment is negligible, laser sheet thickness is enough even though the particle streaks might be longer than the laser sheet thickness. Figure 5.3 shows the schematic of laser sheet generation via glass rod and the actual laser sheet over the flat plate.

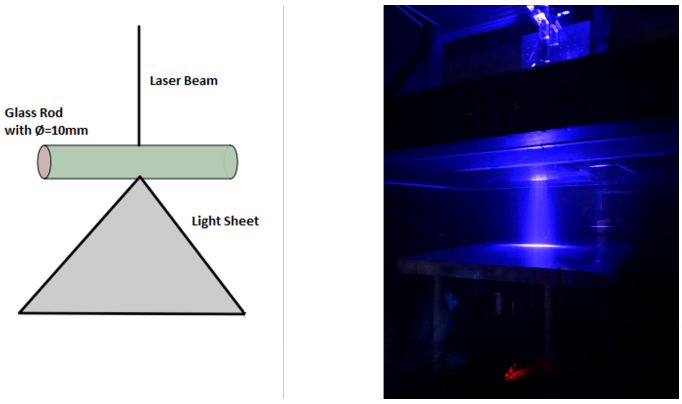

Figure 5.3: Laser sheet in the test section and its generation

When the laser sheet is closely examined, its non-uniformity is noticed due to the existence of dark stripes as it is shown in Figure 5.4. Those dark stripes are the expanded images of dust particles in the laser cavity [14]. The effects of the dark stripes are discussed in Chapter 6. Dark stripes can be eliminated by using a Powell lens instead of a glass rod or cylindrical lens. Also they can be eliminated by rotating the lens [15] but for high sampling rates, rotating the lens at the required speed may not be feasible or even impossible.

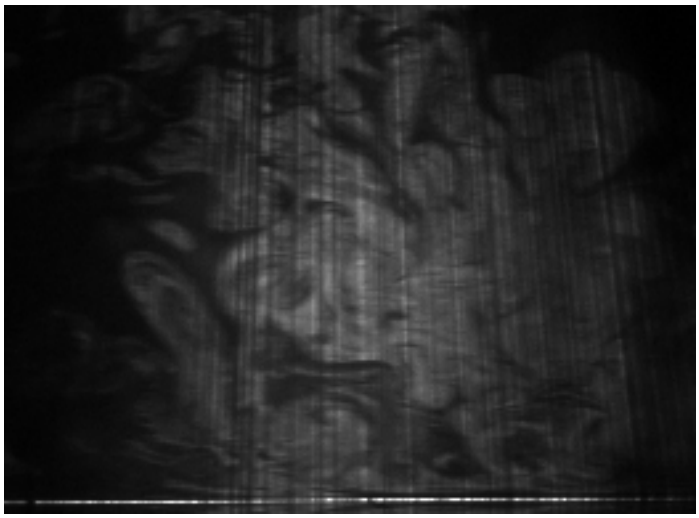

Figure 5.4: Dark stripes on the laser sheet

5.4 Image Recording

Particle images on the ROI are recorded with a *SHIMADZU HYPER VISION HPV-X2* high-speed CMOS camera. A *NIKON* 18-70 mm f/3.5-4.5G ED IF AF-S DX Nikkor Zoom Lens is mounted on the camera (Figure 5.1). In the full-frame mode, frame rate can go up to 5 millions per second meaning that the smallest exposure time is 200 ns. A *FTCMOS2 image sensor* is used in this camera and the resolution is $100,000$ pixels (400 horizontal and 250 vertical). Ten bits, monochrome images are recorded. A Windows compatible control software is provided. The camera's memory can store 128 frames when it is used in the full-frame mode. The half-frame mode can record up to 256 frames at maximum 10 million frames per second; however, it uses 50,000 pixels distributed as a zigzag lattice array which means low resolution.

It is suggested to use the camera in stable environmental conditions (e.g. constant temperature, humidity etc.) in order to minimize the effect of the noise. Noise is observed as dots in the recorded image, appeared to be particles. Therefore, bright dots created by the noise are called *"noise particles"* as if they were dummy particles. Although the reason for this is unknown, in the recorded images, it is noticed that

the noise affects the left-hand side quarter of the frame most but it can be eliminated using an interpolation operator. Figure 5.5 is obtained from *Fluere* [16] software, and it shows an instantaneous vector field which displays this phenomena.

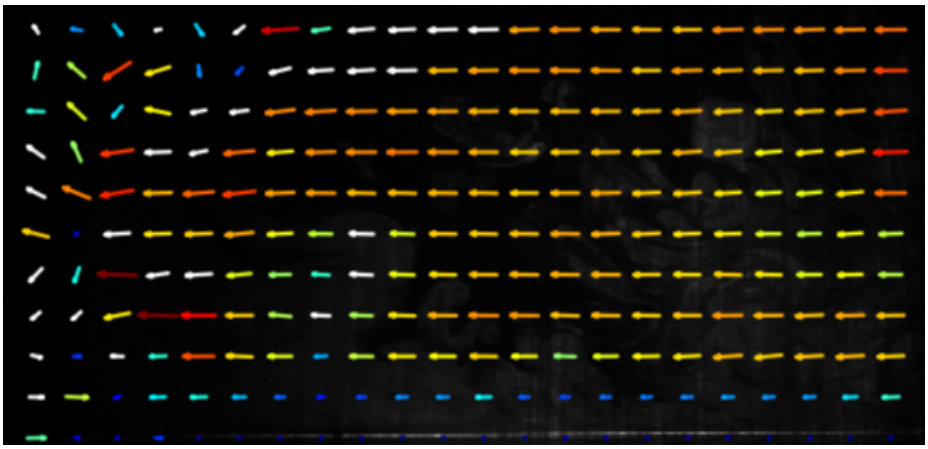

Figure 5.5: The effect of the noise in an instantaneous vector field

Moreover, if the power of the light source is not sufficient, noise becomes an important factor. In other words, if the light scattered from the particles and the brightness of the noise particles are in the same order, it is extremely difficult to distinguish noise and the particle images. Hence, applying noise elimination techniques causes the loss of particle images as well. Further, after the cross-correlation operations, the peaks generated by the particles and the noise particles are comparable; therefore, the post-processing software cannot select the correct correlation peak in order to determine the displacement vector. Selecting the correct peaks manually may be a possible solution; however, it is not practical and having dense seeding conditions may cause additional errors because of particle overlaps.

The exposure time selection affects the amount of light received by the sensor. In other words, more exposure time means more light. If the exposure time is less, particles appear dim, and it is difficult to distinguish noise and particle. On the

other hand, if the exposure time is high, particle streaks becomes longer and they overlap which causes errors. Besides, with high exposure time, displacement vectors are generated as if the particles follow the dark stripes in Figure 5.4. An example is shown in the Figure 5.6. The best results are recorded when the exposure time is 75 μs, and the corresponding streak lengths are tabulated in Table 5.2.

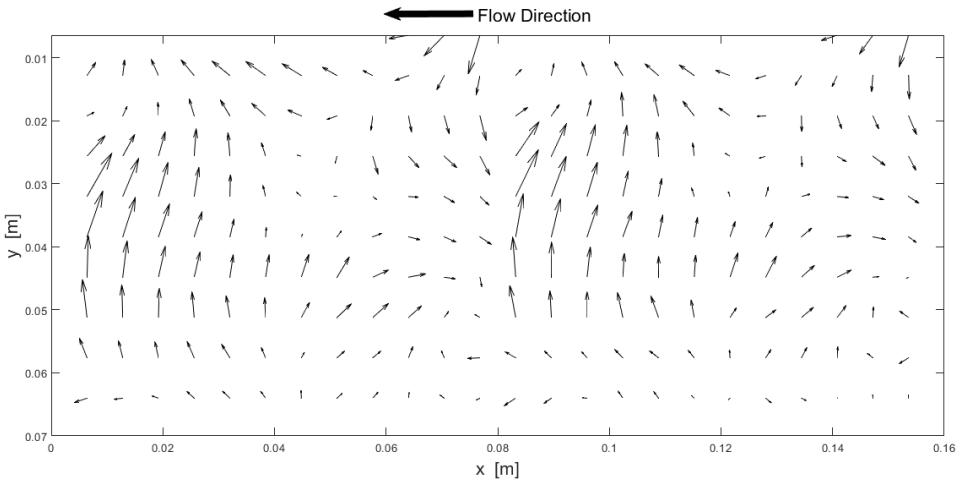

Figure 5.6: Vector field in case of high exposure time

Table 5.2: Corresponding Streak Length for 75 μs of Exposure Time

	Case I (4 m/s)	**Case II (17 m/s)**
Streak Length	0.3 mm	1.275 mm

5.5 Particles

In PIV experiments, flow velocity is calculated. However, this calculation is indirect because in PIV, velocity of the seeding particles are measured directly. In order to have reliable results, particles must faithfully follow the flow. Atomized olive

oil particles are used for seeding in this study. Their dynamics and generation is discussed in following sections.

5.5.1 Particle Dynamics

The equation of the unsteady motion of an infinitesimally small spherical object in a viscous flow is expressed by Maxey and Riley[17] as

$$\begin{aligned} m_p \frac{d\vec{U}_p}{dt} = & -3\pi\mu d_p \vec{U}_r + \frac{1}{6}\pi d_p^3 \left(\rho_p - \rho_f\right)\vec{g} + \frac{1}{6}\pi d_p^3 \rho_f \frac{d\vec{U}_f}{dt} \\ & - \frac{1}{12}\pi d_p^3 \rho_f \frac{d\vec{U}_r}{dt} - \frac{3}{2}\pi d_p^2 \mu \int_0^t \frac{d\vec{U}_r/d\tau}{\sqrt{\pi\mu(t-\tau)/\rho_f}} d\tau \end{aligned} \tag{5.2}$$

where m_p is the mass of the particle, $\vec{U}_r$ is the difference between the particle velocity $\vec{U}_p$ and the flow velocity $\vec{U}_f$, ρ_p is the particle density, ρ_f is the fluid density, g is the gravitational acceleration and μ is the viscosity. On the right-hand side, the first term is Stokes viscous drag, the second term is the buoyant force due to the mass of fluid displaced by the particle, the third is the force on the particle due to velocity gradients of the flow, the fourth one is the force produced by the added mass and the last term is the resistance to the motion caused by the unsteadiness of the flow which is called the Basset history integral [18].

Chao states that in turbulent flows, if the flow density and the particle density are equal, particles follow the flow exactly [19]. In addition to that, Raffel et al. shows that olive oil particles exactly follow the flow after couple of microseconds from their release [12].

5.5.2 Particle Generation

Particles are generated by atomizing olive oil using *LaVision Aerosol Generator* (Figure 5.7) in which the pressurized air at 6 bars drives the liquid olive oil through

the *Laskin Nozzle* so that small droplets are generated. The mean particle diameter for olive oil droplets is given as 1 μm by the manufacturer. If the holes are kept clean, the seeder can sustain particles with constant diameter.

Figure 5.7: Aerosol Generator, Credit: *LaVision*

Particle size determines the smallest scale that can be captured. In other words, the particle size should be smaller than the scale to be measured. In this study, the ultimate aim is to capture the Kolmogorov scale. For Case I, the Kolmogorov scale is slightly larger than the particle size. Since the Kolmogorov scale is inversely proportional to Re, it can not be captured in Case II using olive oil particles.

Since the laser power is not sufficient to scatter enough light from the particles, seeeding intensity is increased in order to increase the resolution but one should be careful about the upper limit of the intensity. In densely seeded flows, particles overlap and cause a lot of error in the post-processing. For particle streaks, this issue becomes even worse. After several trials, optimum density can be set by checking the distance between particle streaks.

Closed circuit wind tunnels like the LSWT in this study, can be filled up with seeding particles and be operated for hours depending on the leak from the tunnel and

deposition on the tunnel wall. This type of seeding is called is "*non-active*" seeding. The other type, which is called "*active*" seeding, is to seed the flow during recording only. Although, it is practical to use non-active seeding, it is not applicable for this experiment due to insufficient laser power. As shown in Figure 5.8, in non-active seeding, particles do not scatter enough light to be detected by the post-processing operations.

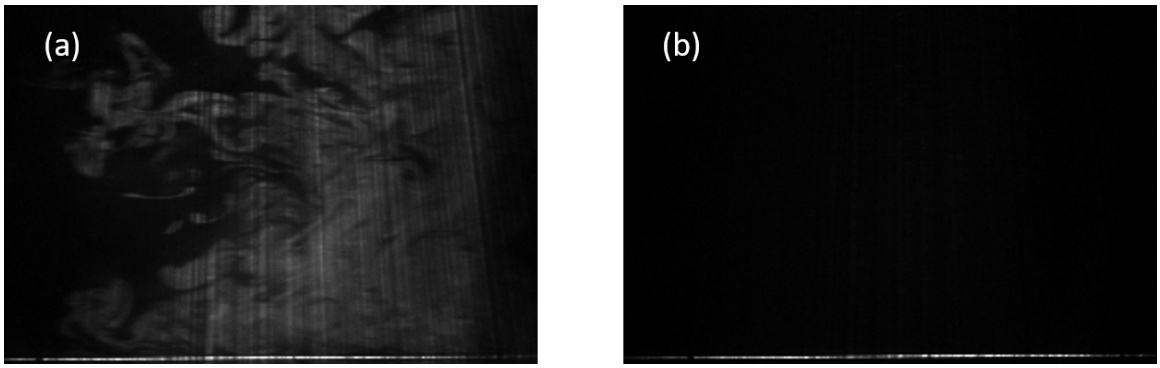

Figure 5.8: Light scattered from the particles in active seeding (a) and non-active seeding (b)

CHAPTER 6

RESULTS

At previously determined sampling rates, the velocity vector fields and the boundary layer profiles are plotted for each case (namely I and II) using *OpenPIV* [9] software. The results are discussed qualitatively and quantitatively. The camera records 128 frames; however, first 3 images are too bright to be used in post-processing. In order to keep the number of frames even so that each image has a pair, only 124 images are analyzed. As was discussed in Chapter 5, the left-hand sides of the frames are more affected by noise. Therefore, spurious vectors are more in this region. This issues is mostly solved by ensembling 124 frames. After ensembling process, invalid vectors are omitted, and their space is filled with interpolated vectors using the neighbor vectors.

Non-ideal PIV images, meaning the images with overlapped particles, gaps, etc., causes data loss and signal drop-out in signal-to-noise ratio (SNR). Therefore, at 10–15 % of data loss is expected [20]. Besides, it is noticed that as the sampling rate increases, data loss increases. It is because the IA size sets the limit wave number, and wave numbers above this value cannot be resolved spatially even though the camera is able to meet the temporal resolution requirements. Generally, the number of valid vectors should be more than 90 % [5] and this is valid for lower sampling rates. However, as the sampling rate increases, the number of invalid vectors increases. Figure 6.1 shows this relation. On the left-hand side, an instantaneous vector field recorded at 150 Hz is shown , and it is noticed that the number of invalid vectors are acceptable whereas on the right-hand side, the vector field recorded at 3 kHz is

shown in which the number of invalid vectors are more than 10 %; hence, causing additional errors.

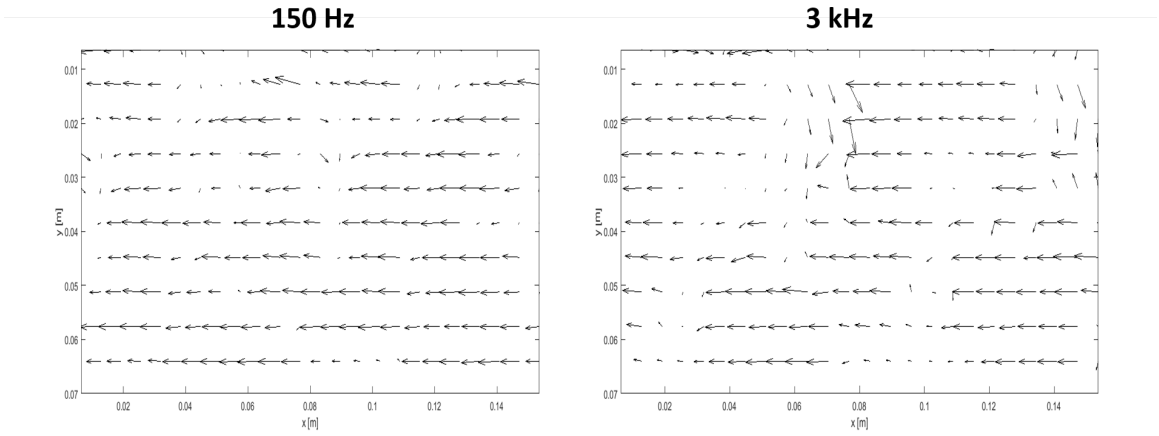

Figure 6.1: Velocity vector maps for different sampling rates

6.1 Case I

In Case I, the freestream velocity ahead of the flat plate is measured as 4 m/s and over the flat plate it is measured as 4.63 m/s. The velocity in the ROI, which is obtained from PIV, is expected to be around 4.63 m/s. The velocity contours are plotted for previously determined sampling rates, which are 150 Hz, 3 kHz and 13 kHz, and Figures 6.2, 6.4 and 6.3 show the contours for these sampling rates respectively.

The first thing to notice in the velocity contours is the spatial resolution problems. Unlike the simulation results in the Figure 4.3, the color distribution in the contours are not uniform. Due to intense seeding, particle streaks overlap and it is difficult to detect the start and the end point of the streak. At the sampling rate of 150 Hz, which is set by the IA size, the PIV system can detect the velocity vector with

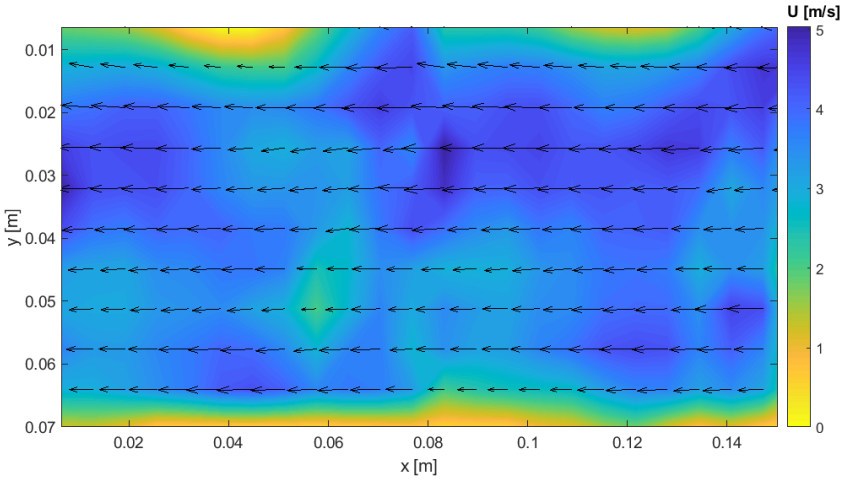

Figure 6.2: Velocity contour for 150 Hz (Case I)

an accuracy of ±10% without any directional ambiguities as illustrated in Figure 6.2. For this case, ensembling and interpolation eliminate the effect of the noise without causing unacceptable errors.

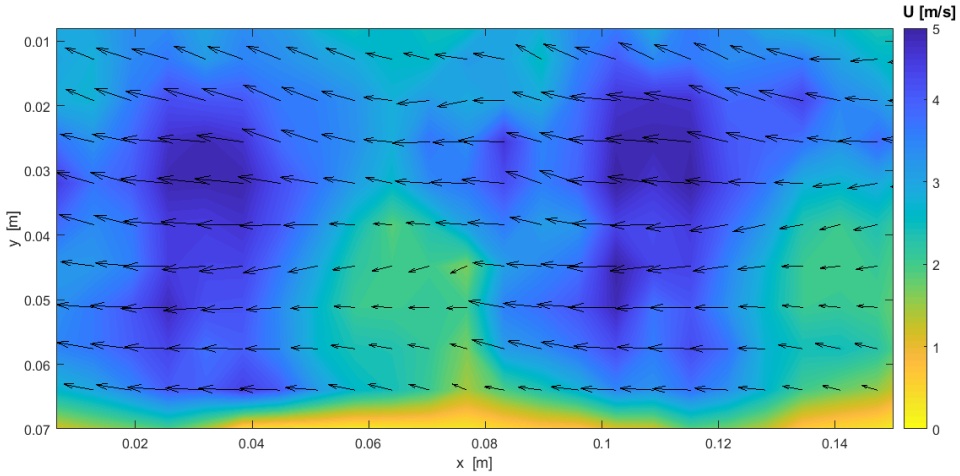

Figure 6.3: Velocity contour for 3 kHz (Case I)

As the sampling rate increases, due to the increase in the number of invalid vectors, associated error increases. Besides, the IA size is larger than the correspond-

ing length scale. Therefore, spatial resolution is not as good as the case with lower sampling rates. Figure 6.3 shows the velocity contour and the vectors obtained from the recordings at 3 kHz. It can be noticed that the accuracy is decreased and directional ambiguities in the velocity vectors are observed. At some points, the velocity measured is half of the actual value.

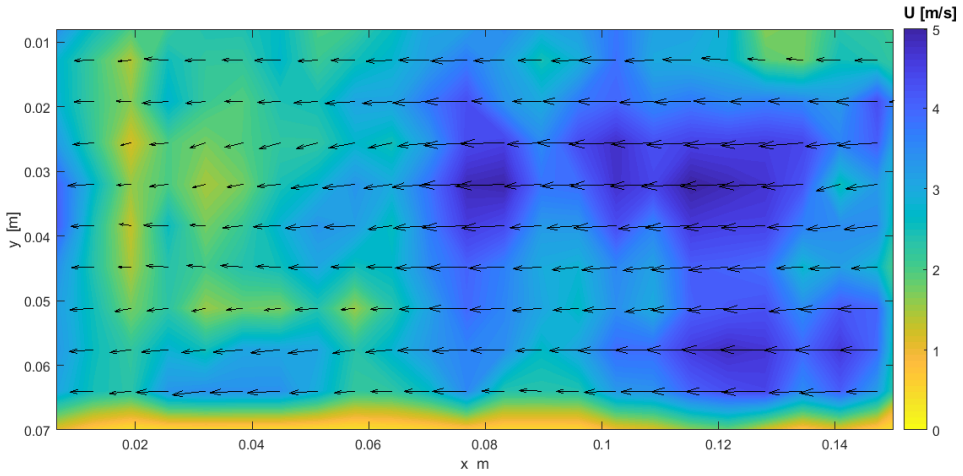

Figure 6.4: Velocity contour for 13 kHz (Case I)

The highest sampling rate for Case I is 13 kHz since it defines the motion of the smallest scale (i.e. Kolmogorov scale) in the flow. Figure 6.4 shows the velocity contour and the vectors measuredt at 13 kHz. Again, due to increased sampling rate, the error further increases. On the left-hand side of the Figure 6.4, the effect of noise could not be eliminated. Further, the velocity measurements are not correct on most of the ROI.

Following velocity measurements, the boundary layer thickness is analyzed on the line located 2 cm right of the mid-line of the ROI. This location is selected due to the error observed in the mid-line of the Figure 6.3. The boundary layer in Case I is laminar since Re is around 72,000 which is lower than the Re_{tr} which is 380,000.

The boundary layer thickness δ at that location was calculated from the simulations in Chapter 4 as 16 mm. The velocity and y distance are normalized with respect to the edge velocity U_e and δ respectively. Then, the boundary layer data of the CFD results and 150 Hz, 3 kHz and 13 kHz measurements are plotted and shown in the Figure 6.5. The measurements at 150 kHz, represented by the red dashed line in the Figure 6.5, are almost identical with the CFD results. However, as the sampling rate increases, the difference between the measured and computed boundary layer profiles becomes significant.

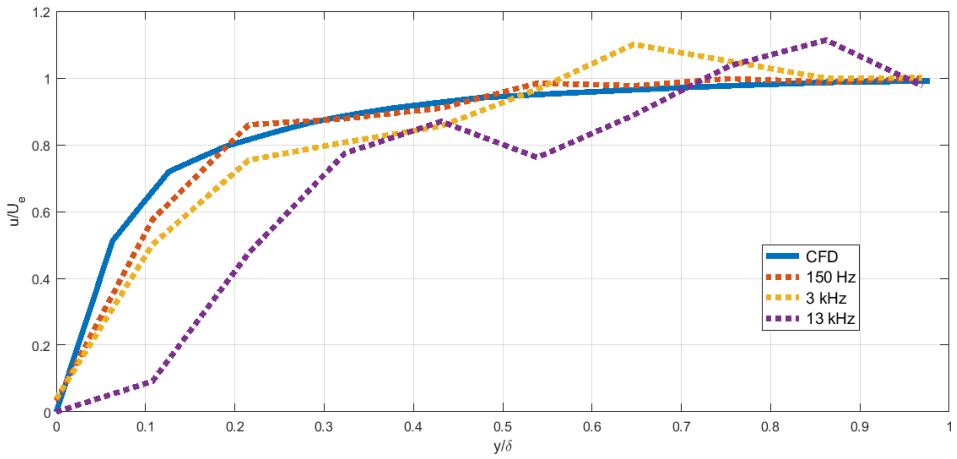

Figure 6.5: Boundary layer profile over the elliptical flat plate (Case I)

6.2 Case II

In Case II, the free-stream velocity is measured as 4 m/s by the pitot-static probe ahead of the flat plate, and over the flat plate it is measured as 17 m/s. The expected velocity in the ROI is around 19.55 m/s. The velocity contours are plotted for sampling rates of 650 Hz and 3 kHz. Figures 6.6 and 6.7 show the velocity contours

for 650 Hz and 3 kHz respectively. The other sampling rates (13 and 54 kHz) are not plotted because of the unacceptable errors obtained in the first two sampling rates.

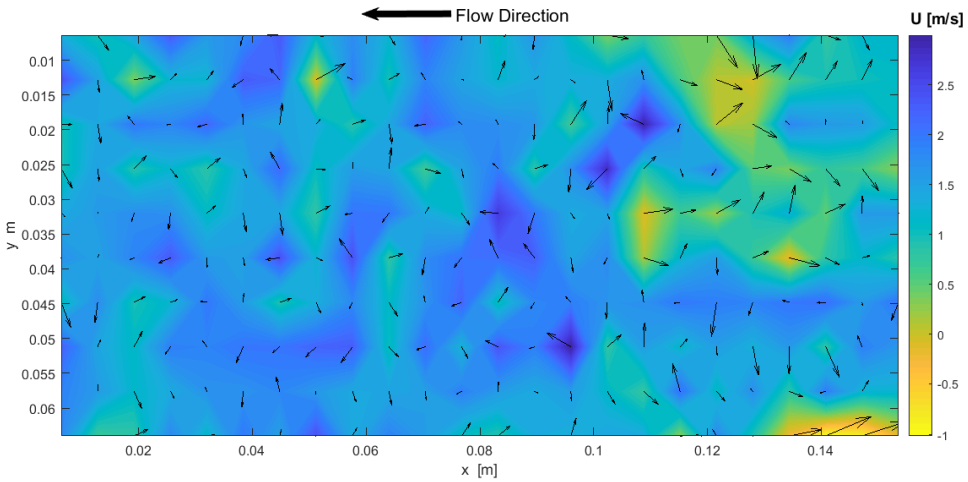

Figure 6.6: Velocity contour for 650 Hz (Case II)

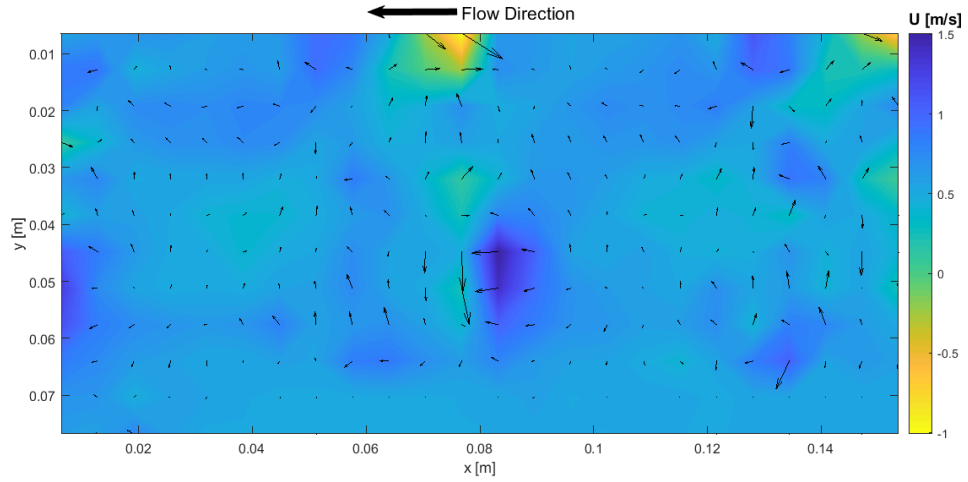

Figure 6.7: Velocity contour for 3 kHz (Case II)

As can be seen in the Figures 6.6 and 6.7, even the flow direction is not captured by the PIV system. The main cause of this issue is the seeding problems

associated with the higher speed. As it was mentioned in the Chapter 5, the flow is actively seeded. Due to the increased speed, the seeding particles are suppressed by the free-stream; hence, the particles could not spread over the ROI. Therefore, the particle density hence the SNR over the ROI remained lower. To increase the particle density, the operating pressure of the aerosol generator is increased; however, this increase caused the generation of very large liquid droplets. In other words, the aerosol generator sprayed olive oil sheets into the test section.

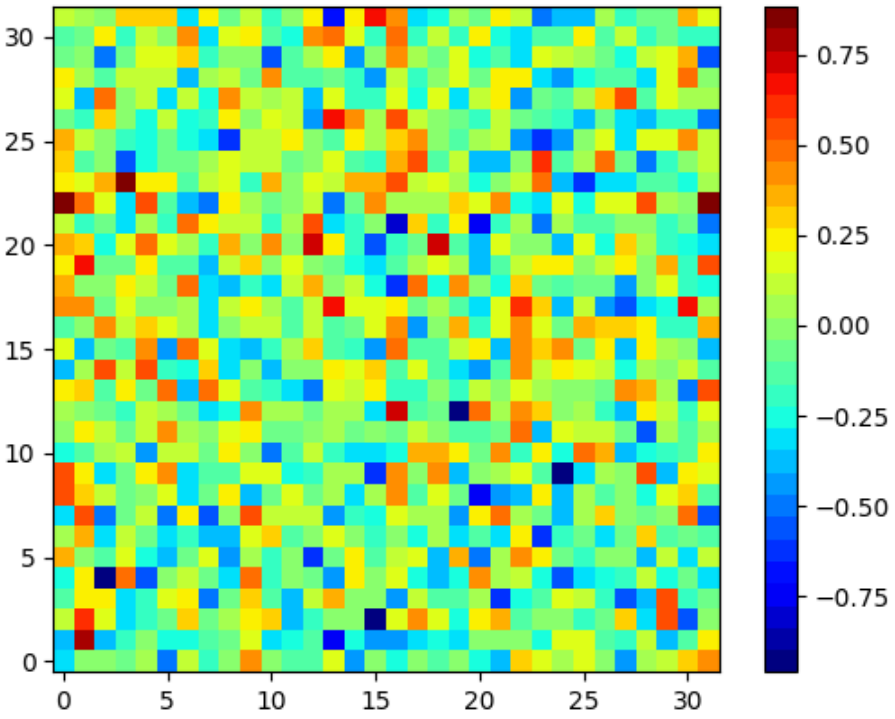

Figure 6.8: Correlation plane for Case II at 650 Hz

Low laser power combined with low particle density caused SNR to drop significantly so that the seeding particles cannot be distinguished from the noise particles.

Figure 6.8 shows an example correlation plane, which is basically a visualized correlation matrix, and in case of this figure, the SNR is 1.09. The dark red squares in the Figure 6.8 represents the highest peak locations. Since the number of the dark red spots are more than one in this figure, it is difficult to determine the actual location of the displacement. Moreover, in some cases, highest peaks might belong to noise. This explains the difficulty of determination of the correct displacement vector in case of low SNR. Because of these issues, velocity data is not calculated for 13 kHz and 54 kHz. Since the velocity data is not accurate, the boundary layer calculations could not be made as well.

CHAPTER 7

CONCLUDING REMARKS AND FUTURE WORK

The PIV system with a continuous-wave laser and high-speed CMOS camera is used in this study. Due to the continuous illumination, particle streaks are generated. The IA size is adjusted so that the particle streak length is in the order of 1 pixel for Case I and 3–4 pixels for Case II. This adjustment allows the usage of particle search algorithms in the post-processes similar to the regular PIV applications. If the particle streak is longer, the start and the end point of the particles has to be detected to calculate the displacement, and the direction of the streak gives the direction of the velocity vector. If the freestream velocity is high, streak length becomes longer. In order to avoid the overlap of the streaks, particle density should be kept lower which causes some gaps in the ROI. Having gaps in the ROI lowers the spatial resolution. To resolve the ROI better and avoid the streak overlaps, lower exposure times should be used. *SHIMADZU HYPER VISION HPV-X2* camera can decrease the exposure time down to 200 ns. For higher speeds, even 200 ns of exposure time may generate longer streaks. For high-speed application, it is suggested to use pulsing lasers to avoid longer streaks. Yet, for low-speed applications, a continuous wave laser offers sufficient and relatively cheap option as an illumination source. Besides, using a continuous laser, eliminates the synchronization of the laser pulses and the camera recordings.

Operating a continuous wave laser means that continuously directing certain amount of energy on to the ROI. Being continuously exposed to high laser energy may cause damages on the test object, and it is not safe for the operators. In addition,

the seeding particles may be flammable; therefore, continuous laser energy may trigger a reaction. A safe operation can be sustained with the continuous-wave laser powers upto 2 W for a short amount of time (around one second) provided that the LIDT limits of the material used are in the safe region. In this study, a 0.5 W continuous wave laser is used. It is observed that the laser power is enough to get accurate results only for limited number of cases due to low SNR. The light scattered by the particles strongly depends on the light source, more than any other parameters [5]. Therefore, the best way to incerase the SNR for this case is to increase the laser power.

Another but less effective way to increase the SNR is to use different types of particles. There are two options for this method. The first one is to use larger particles. Although using larger particles increases the scattered light, it limits the smallest length scale to be captured. The second method is that using particles which scatter the light better such as solid particles. Having smaller size and scattering the light better, solid particles increases the SNR for the PIV setup with a continuous-wave laser and a high-speed camera.

Further, to resolve the ROI better without decreasing its size, more pixels on the camera sensor are required. However, the ROI interest size has to be decreased in order to have better spatial resolution for the given setup. Having smaller ROI may require some surface treatments or image processing to eliminate the surface reflection caused by the light source. Furthermore, the number of frames to be recorded should be increased if the researcher desires to analyze the time history measured parameter.

REFERENCES

[1] Blumer, C. B. and Driest, E. V., "Boundary Layer Transition- Freestream Turbulence and Pressure Gradient Effects," *AIAA Journal*, Vol. 1, No. 6, 1963, pp. 1303–1306.

[2] Barlow, J., Rae, W. H. and Pope, A., *Low-speed wind tunnel testing*, 3rd ed.,Wiley, New York, 1984, pp. 224–227.

[3] Seath, D. D. and Fairchild, J. E. "The University of Texas at Arlington Low-Speed Wind Tunnel,", Arlington, Texas, 1968.

[4] Narasimha, R. and Prasad, S., "Leading Edge Shape for Flat Plate Boundary Layer Studies," *Experiments in Fluids*, Vol. 17, No. 5, Sep 1994, pp. 358–360.

[5] Adrian, R. J. and Westerweel, J. *Particle Image Velocimetry*, 1st ed., Cambridge University Press, 2011, pp. 5, 11, 29, 129.

[6] Dryden, H. L., Schubauer, G. B.,Mock, W. C. Jr.,Skramstad, H. K., "Measurements of Intensity and Scale of Wind-Tunnel Turbulence and Their Relation to the Critical Reynolds Number of Spheres,", NACA TR-581, January 1937.

[7] Dryden H. L., Kuethe, A. M., "Effect of Turbulence in Wind-Tunnel Measurements,", NACA TR-342, January 1931.

[8] Davis, M. R., "Design of flat plate leading edges to avoid flow separation," *AIAA Journal*, Vol. 18, No. 5, 1980, pp. 598–600.

[9] Taylor, Z. J., Gurka, R., Kopp, G. A., and Liberzon, A., "Long-duration time-resolved PIV to study unsteady aerodynamics," *IEEE Transactions on Instrumentation and Measurement*, Vol. 59, No. 12, 2010, pp. 3262–3269.

[10] Willert, C. E. and Gharib, M., "Digital particle image velocimetry," *Experiments in Fluids*, Vol. 10, No. 4, Jan 1991, pp. 181–193.

[11] Bastiaans, R. J. M., "*Cross-correlation PIV; theory, implementation and accuracy"*, EUT Report 99-W-001, Eindhoven University of Technology, Faculty of Mechanical Engineering, Eindhoven, Netherlands, 2000.

[12] Raffel, M., Willert, C., Wereley, S., Kompenhans, J., *Particle Image Velocimetry: A Practical Guide*, 2nd ed., Springer-Verlag, Berlin-Heidelberg, 2007, pp. 16, 169.

[13] Tennekes, H. and Lumley, J. L., *A first course in turbulence*, 1st ed., The MIT Press, Cambridge, MA, 1972, pp. 270, 274.

[14] Tavoularis, S., *Measurement in Fluid Mechanics*, 1st ed., Cambridge University Press, Cambridge, 2005, pp. 318.

[15] Shlien, D. J., "Inexpensive method of generation of a good quality laser light sheet for flow visualization," *Experiments in Fluids*, Vol. 5, No. 5, Sep 1987, pp. 356–356.

[16] Lynch, K. P., "Fluere for Particle Image Velocimetry: User Manual," 2011.

[17] Maxey, M. R. and Riley, J. J., "Equation of motion for a small rigid sphere in a nonuniform flow," *The Physics of Fluids*, Vol. 26, No. 4, 1983, pp. 883–889.

[18] Melling, A., "Tracer particles and seeding for particle image velocimetry," *Measurement Science and Technology*, Vol. 8, No. 12, Dec 1997, pp. 1406–1416.

[19] Chao, B. T., "Turbulent transport behavior of small particles in a turbulent fluid," *Osterreichisches Ingenieur-Archiv*, Vol. 18, No. 7, 1964.

[20] Poelma, C., Westerweel, J., and Ooms, G., "Turbulence statistics from optical whole-field measurements in particle-laden turbulence," *Experiments in Fluids*, Vol. 40, No. 3, 2006, pp. 347–363.

BIOGRAPHICAL STATEMENT

Bunyamin GENCLER was born in Bolu, Turkey, in 1992. He received his Bachelor of Science degree from Middle East Technical University (Ankara, Turkey), in 2017 in Aerospace Engineering. During his undergraduate studies, he worked on low-speed wind tunnel testing, hot-wire anemometry and particle image velocimetry as well as aircraft design, RC model aircraft manufacturing, flight performance and tests in several projects. In Summer 2015, he joined Turkish Aerospace Industries (Ankara, Turkey) as a cooperative education student. In Summer 2016, he completed his internship in Mach Aviation located in Sivrihisar General Aviation Center Necati ARTAN Facilities (Eskisehir, Turkey). In Fall 2017, he joined University of Texas at Arlington to pursue his Master of Science degree in Aerospace Engineering.